Microsc. Microanal. Page 1 of 12
doi:10.1017/S143192761300189X

Microscopy AND Microanalysis

Photobleaching/Photoblinking Differential Equation Model for Fluorescence Microscopy Imaging

J. Miguel Sanches[1,3,*] and Isabel Rodrigues[1,2]

[1]*Institute for Systems and Robotics, Av. Rovisco Pais, Torre Norte, 1049-001, Lisboa, Portugal*
[2]*Instituto Superior de Engenharia de Lisboa-ADEETC, R. Conselheiro Emídio Navarro, 1, Ed. 5, 1959-007, Lisboa, Portugal*
[3]*Department of Bioengineering, Lisbon Institute of Technology, University of Lisbon, Portugal*

Abstract: Fluorescence images present low signal-to-noise ratio (SNR), are corrupted by a type of multiplicative noise with Poisson distribution, and are affected by a time intensity decay due to photoblinking and photobleaching (PBPB) effects. The noise and the PBPB effects together make long-term biological observation very difficult. Here, a theoretical model based on the underlying quantum mechanic physics theory of the observation process associated with this type of image is presented and the common empirical weighted sum of two decaying exponentials is derived from the model. Improvement in the SNR obtained in denoising when the proposed method is used is particularly important in the last images of the sequence where temporal correlation is used to recover information that is sometimes faded and therefore useless from a visual inspection point of view. The proposed PBPB model is included in a Bayesian denoising algorithm previously proposed by the authors. Experiments with synthetic and real data are presented to validate the PBPB model and to illustrate the effectiveness of the model in denoising and reconstruction results.

Key words: photobleaching, denoising, Bayesian, fluorescence microscopy

Introduction

Fluorescence microscopy (FM) images are extensively used in biological and medical research to study processes that occur inside cells. However, intensity fading along the acquisition time, noise due to the photon detection process, and the blur effect due to insufficient resolution of instruments prevent observation of the small, albeit important, details within the specimen. Additionally, when the number of fluorescent molecules is small, high intensity incident radiation is employed to excite the fluorosphores and high amplification gains are needed to make visible the small amount of radiation emitted by them. As a consequence, these images present a low signal-to-noise ratio (SNR), are corrupted by a type of multiplicative noise with Poisson distribution (Dey et al., 2006; Dupé et al., 2008) and are affected by a time intensity decay due to photoblinking and photobleaching (PBPB) effects. The noise and PBPB effects together make long-term biological observations very difficult.

These problems are particularly severe in modalities that use high intensity illumination, such as confocal laser scanning microscopy (CLSM) where the noise and intensity fading along the experiment time are often more limiting than the resolution (see Fig. 1).

This work was motivated by the need to produce high quality images to study synthesis of RNA molecules inside cell nuclei. These molecules are tagged with fluorescent proteins and observed by CLSM. However, the key issue of this article, the PBPB model, is valid for all image modalities where fluorescence intensity decay significantly degrades the observation conditions.

In the literature several models describe this fading effect and among them the single and double exponential laws are the most used. However, a simple and tractable theoretical model based on the physics of the observation process to support these empirical laws is not available.

Here, a theoretical model based on the underlying quantum mechanic physics theory of the observation process associated with this type of image is presented and the common empirical weighted sum of two decaying exponentials (DExp) is derived. The DExp describing the PBPB effects is embedded in a Bayesian denoising algorithm for Poisson data designed to attenuate the noise, increase the SNR of the images, and estimate the underlying morphology in the image.

Improvement in the SNR is particularly important in the last images of the sequence. With this, it is possible to reconstruct the submersed (hidden) underlying morphology from images almost faded out by using information from the previous images in the sequence and vice versa. The reconstruction problem is dealt with as an inverse global problem (Berger, 1985; Bertero & Boccacci, 1998) where the fading intensity law plays a central role.

In the Photobleaching/Photoblinking Model section, a theoretical model for the intensity decay in fluorescence images along the experiment time caused by the PBPB effects, based on physical principles, is proposed. The updated denoising algorithm proposed in Rodrigues and Sanches (2010*b*) for CLSM with the PBPB model is described in the appendix. Synthetic data were generated to test the performance of the proposed algorithm, through a

Received December 7, 2012; accepted May 16, 2013
*Corresponding author. E-mail: jmrs@ist.utl.pt

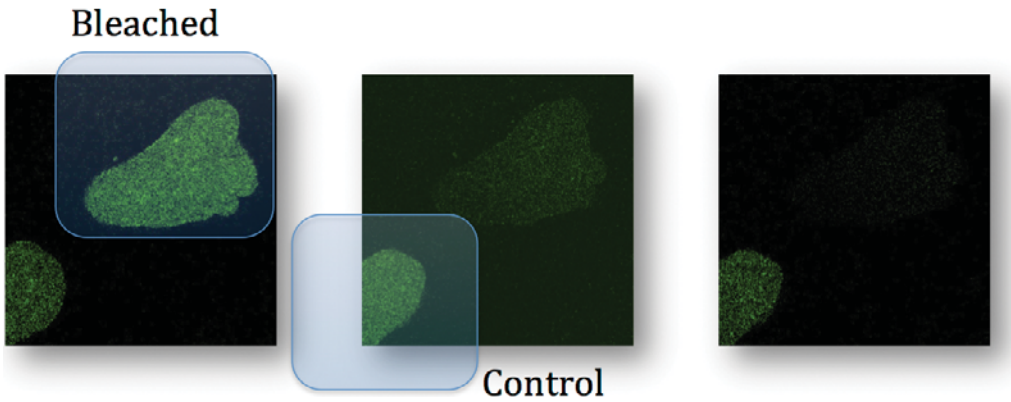

Figure 1. Laser scanning fluorescence confocal microscopy (LSFCM) real image showing a cell nucleus of interest and a control cell nucleus, exhibiting low signal-to-noise ratio and degradation due to nonadditive and non-Gaussian noise as well as the intensity decay along time.

Monte Carlo experiment (see the Monte Carlo Experiments section) and through validation with eight different state-of-the-art algorithms. Real data sequences are then used to illustrate the denoising PBPB compensation ability of the proposed algorithm. Fourth section concludes the article.

Problem Formulation

In this section a model for the PBPB effects in fluorescence images is derived. This model is to be embedded in a Bayesian algorithm to remove the Poisson noise corrupting sequences of fluorescence images. The denoising algorithm where the model is included is described in the appendix and it is an updated version of the one described by Rodrigues and Sanches (2010*b*).

Photobleaching/Photoblinking Model

FM is a powerful biological imaging tool (Lichtman & Conchello, 2005) used to observe *in vivo* dynamic processes occurring inside the specimen, e.g., a cell or cell nucleus. In this technique, tagging proteins, e.g., green fluorescent protein (GFP), fluoresce when radiated with a specific wavelength, making it possible to track single or groups of molecules involved in very specific biochemical processes to be studied.

The radiation emitted by the fluorescent proteins is very weak and its overall intensity decays along the experiment time. This fading effect consists of a temporary, photoblinking, or permanent, photobleaching, loss of the fluorophore ability to fluoresce caused by quanta phenomena associated with the electronic excitation and photochemical reactions among the fluorescent and surrounding molecules, induced by the incident radiation (laser beam in LSCFM imaging), which prevents long-lasting experiments. Thus, the corresponding decay rate depends mainly on the amount of energy radiated over the specimen. Therefore, a trade-off exists between the necessity for increasing the incident radiation to improve the SNR of the image, and the need for decreasing the radiation level to minimize fading effects as well as the phototoxicity.

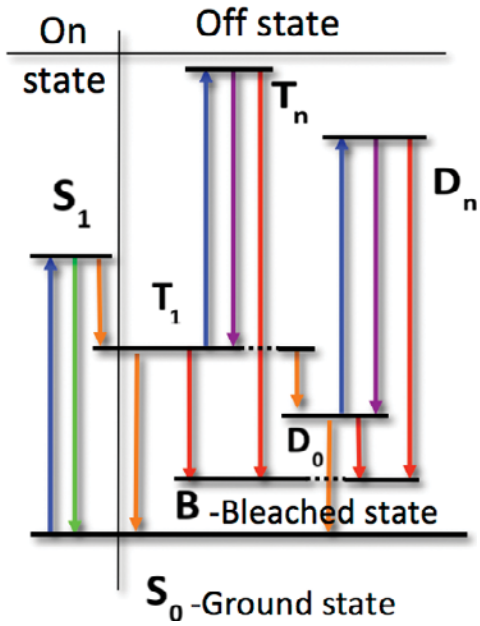

Figure 2. Photoblinking and photobleaching electronic state transition diagram.

An accurate observation model for this intensity decay is essential to obtain effective denoising results in this imaging modality. Different types of photobleaching fitting models have been considered in the literature (Vicente et al., 2007) and among them the most commonly used are the single and multi decaying exponentials.

In this subsection a continuous second-order differential equation dynamic model describing the PBPB effects is proposed. This differential model considers the known quanta phenomena involved in the process that are described in the literature and matches the one that is typically used, and obtained from experimental data (Gavrilyuk et al., 2007; Vicente et al., 2007) where the global intensity decrease along the experiment time is expressed as a weighted sum of two negative exponentials with constant rates.

In this article, fluorescently tagged molecules are assumed to be in one of three main states (see Fig. 2; Didier

et al., 2005): (i) ON-state, where they are able to fluoresce and be observed, (ii) OFF-state, where they are temporarily not able to fluoresce and therefore are not visible, and (iii) BLEACHED-state where they become permanently OFF.

The molecules stay at each OFF-state and ON-state, called active states, according to a power law distribution (Brokmann et al., 2003) and they can commute between these two states; nevertheless, they are not able to recover from the BLEACHED-state. In addition, the average intensity of an image at a given time instant of the experiment is assumed to be proportional to the number of fluorescent molecules at the ON-state.

Here, a continuous time differential equation dynamic model is proposed to describe the number of molecules at the ON-state and OFF-state along the time. This article is a complete and detailed description of the work that was partially described by Rodrigues and Sanches (2010*a*).

Let n be the total number of active fluorescent molecules where n_{on} of them are at the ON-state and the remaining n_{off} are at the OFF-state. The time intervals at each state are governed by the Levy statistics (Brokmann et al., 2003) following a power distribution (Schuster et al., 2007), $p(\tau_s) = c_s \tau_s^{-a_s}$, where $s \in \{on, off\}$, c_s and a_s are constants. The power-law distribution associated with these time intervals is related to the statistical aging effect that leads to a constant increasing of the time intervals between state swaps along the time (Brokmann et al., 2003).

Additionally, it was experimentally confirmed that $a_{\text{on}} > a_{\text{off}}$ (Schuster et al., 2007), which means that the fluorescent molecules spend more time at the OFF-state than at the ON-state, or equivalently, the relative number of transitions from the ON-state to the OFF-state is larger than the relative number of reverse transitions. Therefore, since the molecules spend more and more time at the OFF-state (Schuster et al., 2007), the probability of transitions decreases with time and is always higher from the ON-state to the OFF-state than the reverse.

This nonstationary reversible process of transitions between the ON-state and OFF-state leads to constant image fading along the experiment time called photoblinking. Photobleaching, on the other hand, is a nonreversible process where the fluorescent molecules loose their ability to fluoresce.

As noted in Didier et al. (2005) the transitions to the permanent dark states occur only from the excited states. Here, however, the model proposed in Zondervan et al. (2004) is adopted, where photobleaching from the ON-state is discarded. In this model, displayed in Figure 2, it is assumed that no photobleaching occurs from the excited singlet state, S_1 but only from the OFF-states, composed by the triplet, T_n, and anion, D_n, states. Transitions to the permanent dark states, represented by the red arrows in the Jablonski diagram displayed in Figure 2, suggest the following set of differential equations to describe the dynamics of the PBPB effects:

$$n(t) = n_{\text{on}}(t) + n_{\text{off}}(t), \tag{1}$$

$$\frac{dn_{\text{on}}(t)}{dt} = \beta_{\text{off}}(t) n_{\text{off}}(t) - \beta_{\text{on}}(t) n_{\text{on}}(t), \tag{2}$$

$$\frac{dn(t)}{dt} = \xi n_{\text{off}}(t), \tag{3}$$

where $n(t)$ is the total number of active molecules at instant t and $n_{\text{on}}(t)$ and $n_{\text{off}}(t)$ are the number of active molecules at the ON-state and OFF-state respectively, at the same instant. $\xi = I + \tau$ is the decay rate of the active molecules associated with transitions to the permanent BLEACHED-state, where I is proportional to the amount of incident radiation and τ is associated with other factors not related to illumination. This means that even when no radiation illuminates the specimen, $I = 0$, the number of active molecules decreases. However, since the main factor for the intensity decay is the incident radiation, it is expected that $I \gg \tau$.

Equation (2) models the photoblinking effect where it is assumed that the variation of the number of molecules at the ON-state is proportional, with constant β_{off}, to the number of molecules at the OFF-state and negatively proportional, with constant β_{on}, to the number of molecules at the ON-state.

The magnitudes of β_{on} and β_{off} are related with the previously referred to statistical aging effect (Brokmann et al., 2003) that leads to an increasing number of active molecules at the OFF-state and an identical decreasing number at the ON-state. Therefore, the transition rate from the OFF-state to the ON-state is smaller than the inverse transition, which means that $\beta_{\text{on}} > \beta_{\text{off}}$.

Equation (3) models the photobleaching effect where it is assumed that the total variation on the number of active molecules is proportional, with constants τ and I, to the number of molecules at the OFF-state, because only transitions from the OFF-state to the BLEACHED-state are admissible at the model proposed in this chapter (see red arrows in Fig. 2).

According to Didier et al. (2005), the main cause for photobleaching is the "illumination history." However in Zondervan et al. (2004) other important factors for photobleaching to occur are referenced, such as the humidity and the temperature. The overall effect of these factors is modeled in equation (3) by the constant $\tau \ll I$. From the set of equations (1)–(3) the following second-order differential equation describes the dynamics of the number of molecules at the ON-state, directly related to the intensity of the image:

$$\frac{d^2 n_{\text{on}}(t)}{dt^2} + (\alpha + \xi) \frac{dn_{\text{on}}(t)}{dt} + \beta_{\text{on}} + n_{\text{on}} + (t) = 0, \tag{4}$$

where $\alpha = \beta_{\text{on}} + \beta_{\text{off}}$.

The Laplace transform of $n_{\text{on}}(t)$ for the initial conditions $n_{\text{on}}(0) = n_{\text{on}}^0$ and $dn_{\text{on}}(0)/dt = \dot{n}_{\text{on}}^0$ is

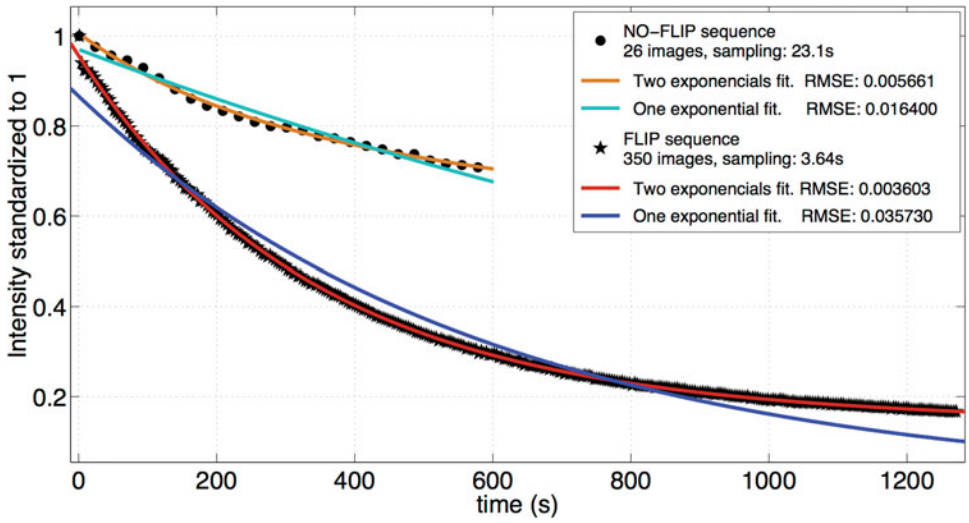

Figure 3. Standardized average intensity per image as a function of the experiment time, for two laser scanning fluorescence confocal microscopy real data sequences, one without using fluorescence loss in photobleaching (FLIP) nor any other technique (dark circles) and the other using the FLIP technique (dark stars). Red and orange curves stand for the fits of the data with two-exponentials models. Blue and cyan curves stand for the fits of the data with one-exponential models. The root mean square error is displayed in the plot legend. Data provided by the Instituto de Medicina Molecular (UL) Lisbon.

$$N_{\text{on}}(s) = \frac{as + b}{(s + \lambda_1)(s + \lambda_2)}, \tag{5}$$

where $a = n^0_{\text{on}}, b = (\alpha + \xi)n^0_{\text{on}} + \dot{n}^0_{\text{on}}$ and

$$\lambda_{1,2} = \frac{\alpha + \xi}{2} \mp \frac{\sqrt{\Delta(\xi)}}{2}, \tag{6}$$

with discriminant

$$\Delta(\xi) = \xi^2 - 2\underbrace{(\beta_{\text{on}} - \beta_{\text{off}})}_{>0}\xi + \alpha^2. \tag{7}$$

The roots of equation (7), $\xi_{1,2} = \beta_{\text{on}} - \beta_{\text{off}} \pm 2\sqrt{-\beta_{\text{on}}\beta_{\text{off}}}$ are always complex because $\beta_{\text{on}}, \beta_{\text{off}} > 0$. Therefore, the discriminant equation (7) is always positive, $\Delta(\xi) > 0$, which means that the poles $\lambda_{1,2}$ are always real. The inverse Laplace transform of equation (5) is

$$n_{\text{on}}(t) = \gamma e^{-\lambda_1 t} + (\alpha - \gamma)e^{-\lambda_2}, t \geq 0, \tag{8}$$

where

$$\gamma = \frac{a\lambda_1 - b}{\lambda_1 - \lambda_2}. \tag{9}$$

The intensity decay law described by equation (8) and derived from equations (1)–(3) matches the experimental model referred to in the literature where the PBPB global effect is expressed in terms of the linear combination of two decaying exponentials.

Figure 3 shows the evolution of the average intensity per image, where time is in seconds, for two real data sequences, one acquired without using any CLSM technique and the other using the fluorescence loss in photobleaching (FLIP) technique (see the Real Data section for a short description of this technique). As can be observed in this figure, the fits of the data using two-exponentials models (red and orange curves) yield better results than the one-exponential models (blue and cyan curves). Also the values of the root mean square error (RMSE) displayed in the plot legends confirm this assertion.

Experimental Results

In this section experimental results using synthetic and real data are presented. The proposed PBPB model is embedded in the denoising algorithm described in Rodrigues and Sanches (2010*b*), and the results are compared with some of the state-of-the-art algorithms described in the literature as well as with a previous version (Rodrigues & Sanches, 2010*b*) where the PBPB model is not considered.

In the Model Validation section, the validation of the proposed algorithm with several state-of-the-art ones is performed. The results are displayed and discussed.

Synthetic Data

The synthetic data used in this article consist of a sequence of 64 images, 64 × 64 pixels each, where two squares, one inside the other, slide along the images diagonally, as suggested in Figure 4. The intensity values of the original sequence were set to attain SNR values between 4.5 and 12.2 dB in the noisy data. The sampling interval is assumed to be 1 s.

This moving synthetic morphology, with two intensity layers, was faded out with a two exponentials decay, $\eta(t) = 0.1e^{-\lambda_1 t} + 0.9e^{-\lambda_2 t}, t = (0,\ldots,63)$, with rates $\lambda_1 = 0.04\ \text{s}^{-1}$ and $\lambda_2 = 0.0025\ \text{s}^{-1}$, to simulate the global PBPB effect. This sequence is used to illustrate the performance of the method and how it copes with sharp intensity transitions along with moving features inside the specimen and with low SNR.

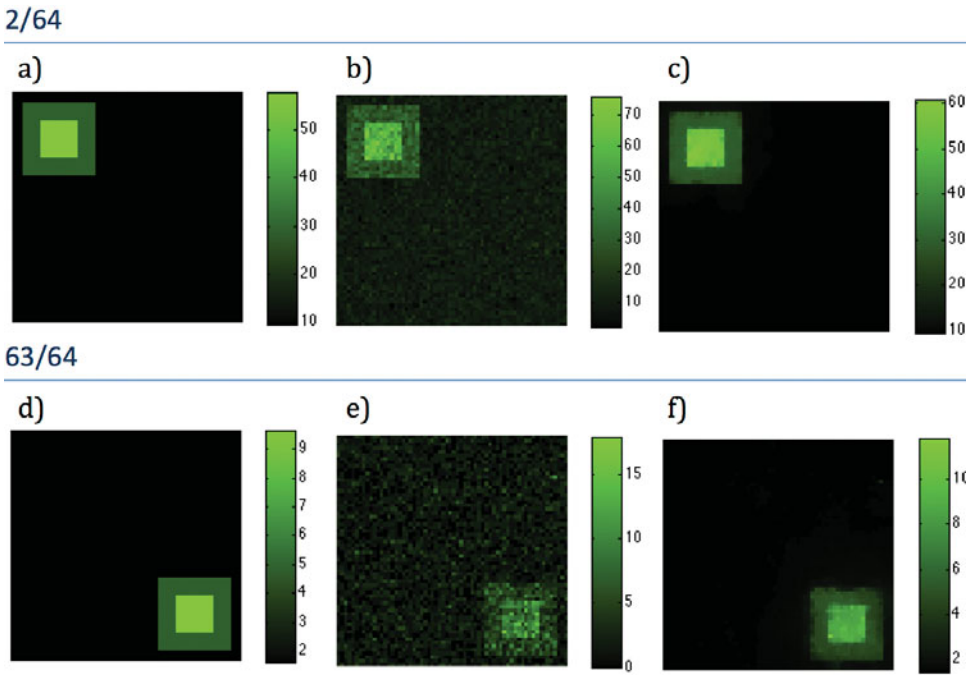

Figure 4. Images 2 and 63 from 64 of the synthetic sequence. Original images (**a**, **d**), corrupted (**b**, **e**), and denoised (**c**, **f**).

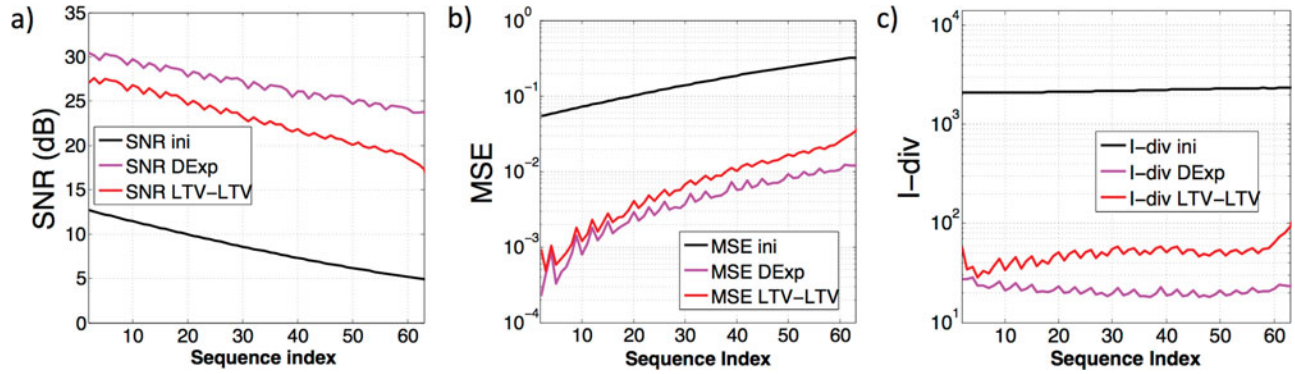

Figure 5. **a–c**: Respectively signal-to-noise ratio, I-divergence, and mean square error results per image, of a Monte Carlo experiment in 500 runs, for the denoising algorithms with no photoblinking and photobleaching compensation (red), and with the two-exponentials compensation (pink). The black line stands for these quality quantifiers before applying any of the algorithms.

Figure 4 displays the corresponding images at two different times, one at the beginning and the other at the end of the sequence, where the degradation is more visible. This figure displays for each instant the original noncorrupt image we want to estimate, the corresponding observed corrupted images, and finally the estimated images.

The performance quantification of the algorithm is accessed using the SNR the mean square error (MSE) and the Csiszár's I-divergence (I-div) (Csiszáer, 1991).

The model regularization parameters α and β [equation (A.14)], strictly positive, are tuned in a trial and error basis.

Monte Carlo Experiments

In this subsection a Monte Carlo test is presented to access the performance of the proposed algorithm, using the generated synthetic data described in the Synthetic Data section. The Monte Carlo test was carried on the sequence, in 500 runs with 500 iterations each. A run consists of loading the original sequence, corrupting it with Poisson noise, completing 300 iterations of the denoising algorithm and computing the results of the SNR, I-div, and MSE quality quantifiers. Averages and standard deviations of these figures-of-merit (FOMs) are computed over all runs.

The SNR, I-div, and MSE results of the Monte Carlo experiment for the synthetic sequence are displayed in Figure 5, where an improvement of ∼20 dB is achieved along the sequence. In this figure, the FOMs obtained with the method proposed by Rodrigues and Sanches (2010*b*), here called LTV-LTV, are also displayed for comparison purposes. The inclusion of the PBPB model leads to an improvement of ∼3 dB in the initial images of the sequence. This improvement increases along the sequence making it possible to attain larger gains in the last images where the degradation is more severe, as shown in Figures 5a and 5b.

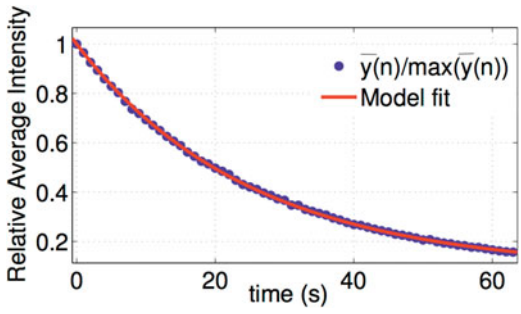

Figure 6. Fit of the two-exponentials photoblinking and photobleaching compensation curve, computed in one of the Monte Carlo experiment runs.

The parameters of the photobleaching compensation curve, in this experiment with synthetic data, were assumed unknown and were estimated using equation (A.5). The results of the fitting are displayed in Figure 6 and show good agreement with the true values, corresponding to the following model: $\eta(t) = \psi_1 e^{-\lambda_1 t} + (1 - \psi_1)e^{-\lambda_2 t}$. Coefficients with 95% conf. bounds: $\lambda_1 = 0.11(0.12, 0.11)$, $\lambda_2 = 0.0028(0.0018, 0.0038)$, $\psi_1 = 0.041(0.04063, 0.04136)$. Goodness of fit: SSE $= 596.1 \times 10^{-6}$, $\bar{R}^2 = 0.9998$, RMSE $= 0.0031$.

Model Validation

The synthetic sequence was processed with the proposed algorithm and with the following eight state-of-the-art algorithms described in the literature:

- naive Gauss proximal iteration using curvelets (Prox-it-GaussCURV) (Dupé et al., 2009)
- naive Gauss proximal iteration using wavelets (Prox-it-GaussWAV) (Dupé et al., 2009)
- Anscombe proximal iteration using wavelets (Prox-it-Ans-WAV) (Dupé et al., 2009)
- Anscombe proximal iteration using curvelets (Prox-it-Ans-CURV) (Dupé et al., 2009)
- nonlocal means (NLM) (Buades et al., 2005)
- bilateral filtering (Tomasi & Manduchi, 1998)
- constant, wedgelet, and platelet fitting-based model (PLAT) (Willett, 2006)
- Haar-TI hereditary (Haar-TI) (Willett & Nowak, 2004*a*, 2004*b*).

In order to make the validation as fair as possible, whenever feasible, the parameters of the comparison models were adjusted from image to image, to account for decreasing of the intensity along the sequence to obtain the best possible results. The parameters of the PBPB model were assumed unknown and were estimated as explained in the Denoising Results section. The Csiszáer I-div and the SNR, used here as quality metrics, were computed for each image and the plots are displayed in Figures 7 and 8. The superior performance of the proposed algorithm when dealing with sequences exhibiting a low SNR, corrupted with Poisson noise and presenting a fading effect of the intensity along the time is noticeable in these plots.

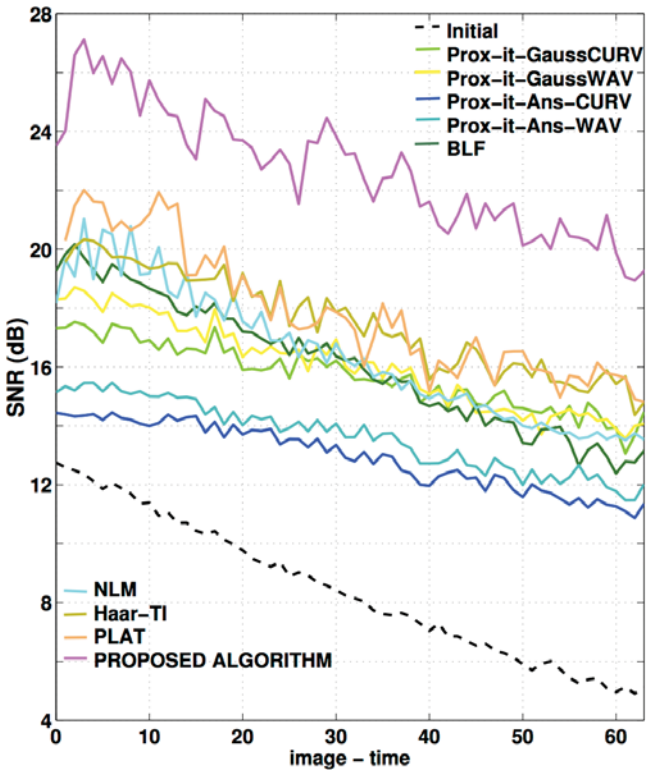

Figure 7. Signal-to-noise ratio for all the comparison algorithms and the proposed one.

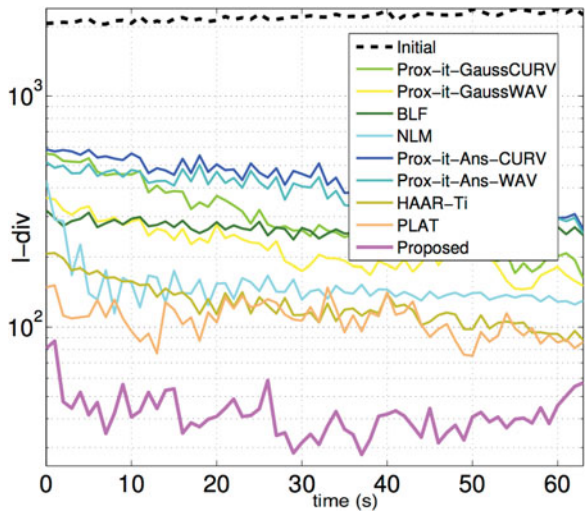

Figure 8. Csiszár I-divergence for all the algorithms using the synthetic data.

The NLM model also performs very well. Against all odds, both versions of the Prox-it-Ans perform very poorly, perhaps due to the fact that the involved tuning parameters, estimated according to the generalized cross validation criterion (Dupé et al., 2009), are not the best ones to cope with the lack of blur in the sequence.

The relative error (RE) between consecutive iterations, used as stopping criterion for the proposed convex algorithm, is computed as

Table 1. CPU Time to Denoise the 64 Images of the Synthetic Sequence.*

Algorithm	CPU Time (s)	Image 2 SNR (dB)	Image 2 MSE	Image 58 SNR (dB)	Image 58 MSE
Proposed	17.2	25.6	0.003	19.0	0.01
Haar-T1	2.2	20.1	2.2	15.6	0.2
BLF	18.3	19.8	2.4	13.2	0.4
NLM	147.9	22.5	1.3	16.5	0.2
Prox-it-Gauss CURV	14,417.6	0	0	0	0
PLAT	1,319.2	21.5	1.6	16.1	0.2
Prox-it-Ans CURV	1,853.4	0	0	0	0
Prox-it-Gauss WAV	971.2	18.3	3.3	14.4	0.3
Prox-it-Ans WAV	14,417.6	0	0	0	0

*The dimensionality of the algorithms is displayed.
BLF, Bilateral filtering; SNR, signal-to-noise ratio; MSE, mean square error; NLM, nonlocal means; PLAT, platelet fitting-based model.

$$\mathrm{RE} = \frac{\|z^{(k)} - z^{(k-1)}\|}{\|z^{(k)}\|} \leq 0.5 \times 10^{-4}. \tag{10}$$

All the algorithms were executed under the same conditions and the processing times as well as the SNR and MSE for images 2 and 58 are listed in Table 1. The proposed algorithm, with prior parameters optimized in a trial and error basis, outperforms all of the others and is the second fastest one.

Real Data

The data used in this work are LSCFM images of Hela (Jackson et al., 1998) *in vivo* cell nucleus. The real data sequence, denoted by 2-G100, consists of 100 images, 130 × 140 pixels each (scale 0.03 μm) and sampled at a rate of 23.1 s.

The present work was motivated by this need to study transport and diffusion processes that occur inside the cell nucleus. In human cells, messenger ribonucleoproteins (mRNP), after being released from the transcription sites and distributed throughout the nucleoplasm, must reach the nuclear pore complexes in order to be translocated to the cytoplasm. To study the nature of this transport, quantitative photobleaching methods can be used to determine the mRNP's mobility inside the nucleus of living cells.

In the acquisition process of image sequences used in this article, RNP complexes were made fluorescent by transient expression of GFP fused to two distinct mRNA-binding proteins: PABPN1 and TAP (Molenaar et al., 2004; Vargas et al., 2005) and the FLIP technique (Underwood, 2007; Rino et al., 2009) was used. This technique makes use of high intensity laser light as a perturbing agent of the distribution of fluorescent molecules in the cell nucleus. In a FLIP experiment, during a certain time interval, a small target region within the nucleus, expressing fluorescently tagged proteins, is illuminated with repetitive pulses of a high intensity focused laser beam, in order to force the occurrence of the photobleaching effect in that region.

Table 2. Real Image of Sequences.*

Real Data	Two Exponentials $\hat{\lambda}_1 \times 10^{-4}$ (s^{-1})	%	$\hat{\lambda}_2 \times 10^{-4}$ (s^{-1})	%
BDM-FLIP	31.04	83	3.604	17
2-G100	29.10	62	1.600	38

*Estimated parameters for the photoblinking and photobleaching models with two exponentials.

An area away from the target is then monitored for a decrease in the level of fluorescence. Any fraction of the cell nucleus connected to the area being bleached will gradually fade owing to the movement of bleached molecules out of the bleached region.

The resulting information from the experiment can then be used to determine the kinetic properties of the fluorescently labeled molecules. The drawback of applying this technique is the fast degradation of the images along the experiment time, worsened by the global photobleaching effect.

The data set, denoted by BDM-FLIP, is the result of a FLIP experiment where a target spot of 1.065 μm radius (30 pixels diameter) in the cell nucleus was repeatedly bleached by 279 ms pulses, at intervals of 3.64 s and imaging between pulses using low intensity light. This sequence consists of 350 images, 300 × 380 pixels each (scale: 0.07 μm).

No preprocessing, such as background subtraction, was performed on these real data images but a simple alignment procedure to correct for cell nucleus displacement during the acquisition process was performed. A mask of the region of interest (the cell nucleus) was obtained from the aligned sequence by a segmentation procedure, with the purpose of running the denoising algorithm only inside the cell nucleus, saving memory and CPU time.

In order to estimate the nucleus morphology F, the aligned images were then processed using the proposed denoising with photobleaching compensation methodology.

The average per image of each sequence was computed and is displayed in Figure 10.

Denoising Results

The set of real CLSFM images, identified as 2-G100, was denoised with the proposed algorithm. The results are shown in Figure 9.

Three images, 1, 20, and 45 of sequence 2-G100, corresponding to the time instants 0, 460 and 1,035 s of the acquisition process, are displayed in the first row Figure 9a. The appearance of these images is very noisy and the intensity fading along the time is perfectly noticeable. In fact, in the last images of the sequences it is very hard to see the cell nucleus.

The rates of decay due to photobleaching were estimated and so were the cell nucleus morphology, $\hat{F} = \{\hat{f}_{i,j,t}\}$ and the reconstructed images $\hat{X} = \{\hat{x}_{i,j,t}\}$ using both versions of the PBPB model. The results for the rates of decay are in Table 2.

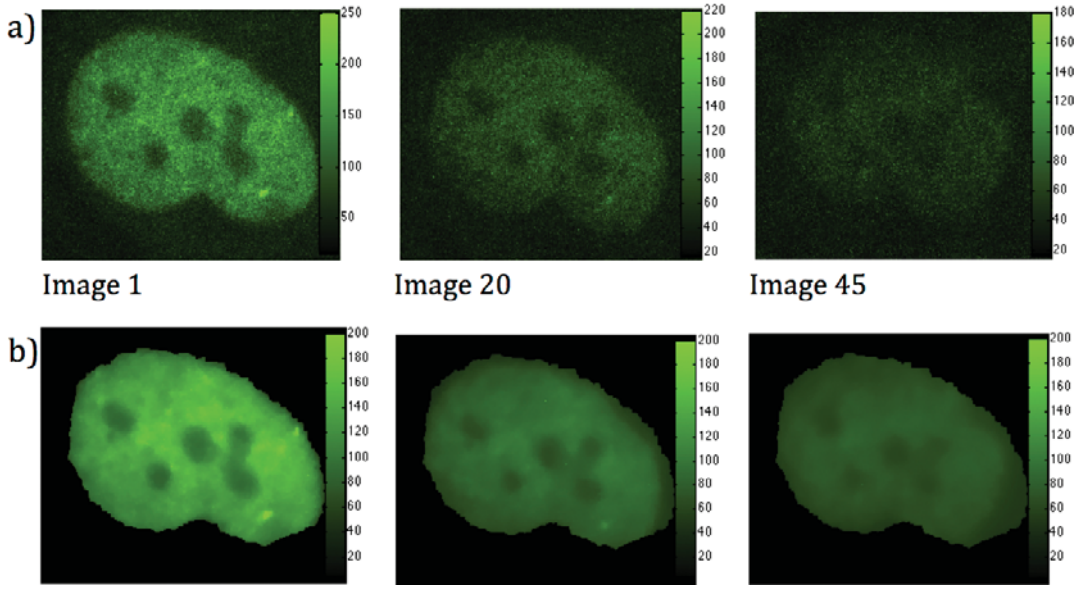

Figure 9. Real sequence: 2-G100. Proposed algorithm with DExp PBPB model. (**a**) Noisy images 1, 20, 45 from the real data set and (**b**) respective reconstructed images.

In Figure 9b, images of the reconstructed sequence for the same time instants as in Figure 9a can be seen. A considerable reduction of the noise while the morphological details are still preserved is noticeable.

Improvement in the quality of the details of the cell nucleus structure even when almost no information is available (compare first and third rows) is also substantial.

The average of the images of the noisy and reconstructed sequences, using the proposed algorithm, were computed and the results are presented in Figure 10. As can be observed, the average of the reconstructed images is well preserved.

In order to test the behavior of the proposed two-exponentials algorithm in more complex situations where diffusion and transport phenomena are present, the sequence BDM-FLIP, which is the result of applying the FLIP technique to the Hela cell nucleus, is used.

Three images from this sequence ($t = 29.6$, 362.6, and 843.6 s) and respective image reconstructions are displayed in Figure 11. The intensity decrease is quite fast, making the acquisition very difficult for long exposures.

Estimated values of the rates of decay of the intensity obtained with the two-exponentials PBPB model are displayed in Table 2. Improvement in the details of the nucleus structure is noticeable both in the reconstruction and in the morphology. The values of the rates of decay attained for this sequence are obviously larger than the ones obtained for sequence 2-G100, due to the use of the FLIP technique that reinforces the decrease of the intensity.

The CPU time the proposed algorithm takes to process each sequence in a Centrino Duo 2.00 GHz, 1.99 GB RAM processor, along with the corresponding number of iterations are displayed in Table 1. The applied stopping criterion is based on the RE per iteration [see the Model Validation section, equation (A.1)] set to RE $\leq 5 \times 10^{-5}$.

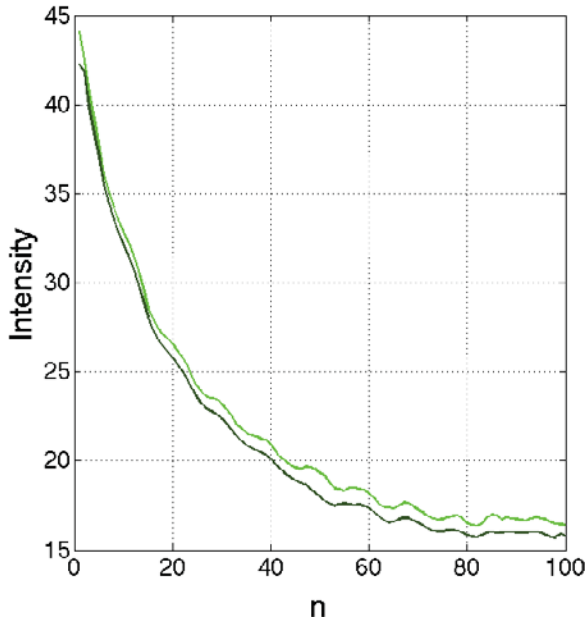

Figure 10. Real sequence: 2-G100. Average intensity per image of the real sequence. Dark and light green lines correspond to the reconstructed and to the noisy sequences, respectively.

CONCLUSIONS

Sequences of fluorescence images, especially sequences of CLSM images where high intensity laser radiation illuminate the specimen, are corrupted by a type of multiplicative noise, usually assumed to be described by the Poisson distribution, and the global intensity of the images decreases along the time due to permanent fluorophore loss of its ability to fluoresce. This fading effect, called photoblinking/photobleaching, is caused by chemical reactions induced by the incident radiation and by other surrounding molecules.

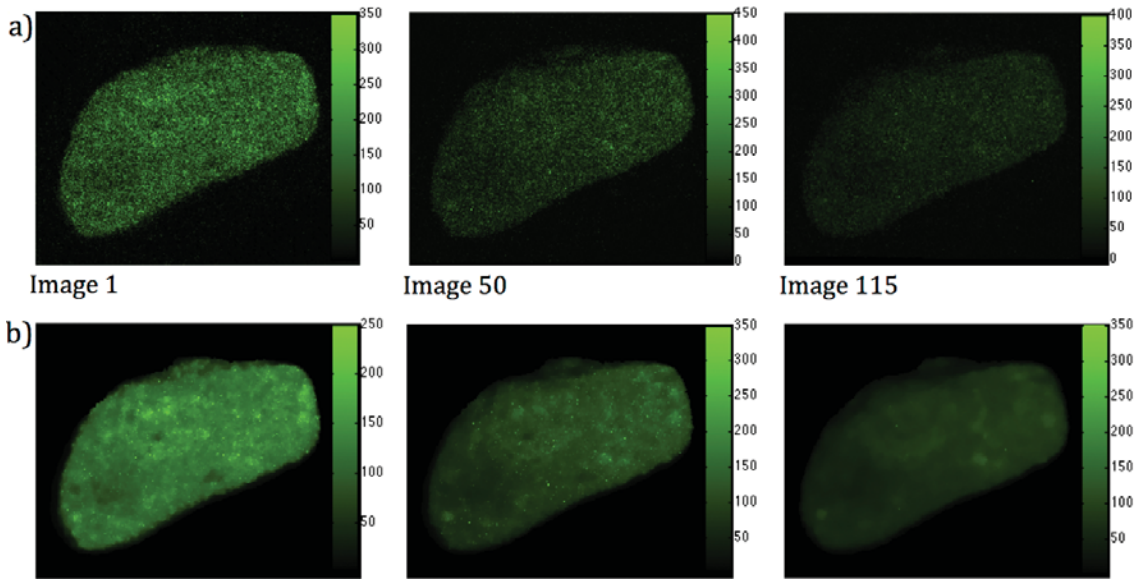

Figure 11. Real sequence BDM-FLIP. Proposed algorithm with DExp PBPB model. (**a**) Noisy images 5, 50, 115 from the real data set and (**b**) respective reconstructed images.

PBPB leads to a decrease in the SNR of the images, which prevents long-term observation experiments and makes biological information recovery a difficult task.

In this article, a novel differential equation model is proposed to describe the PBPB effect. The common empirical weighted sum of two decaying exponential usually referred in the literature is derived from the theoretical model, based on the underlying quantum mechanic physics theory of the observation process associated with these types of images.

The model is included in a denoising algorithm developed in a Bayesian framework that performs denoising simultaneously in space and time dimensions. The formulation involving a 2D time anisotropic filtering procedure, where an energy function is designed to be convex, and its minimizer is computed by using Newton's algorithm and an iterative reweighted least-squares-based method, which allows convergence toward the global minimum in a few seconds. In the proposed formulation the PBPB effects are explicitly taken into account by using a two-exponentials model derived from the proposed model.

Tests using synthetic and CLSM real data reveal the ability of this methodology to reduce the multiplicative noise corrupting the sequence. Furthermore, several previous version of the presented model with and without PBPB compensation and using different *a priori* potential functions are also briefly described. Results of their use through Monte Carlo experiments are compared with the ones obtained with the proposed model. The proposed model outperforms its previous versions in every situation, mainly due to its edge preserving properties and to the explicit embodying of the PBPB compensation in the model. Validation of the proposed model with several state-of-the-art models confirms the good performance of the proposed methodology.

Acknowledgments

The authors thank Dr. José Rino and Prof. Maria do Carmo Fonseca, from the Institute of Molecular Medicine of Lisbon, for providing biological technical support and the real data used in this article. This work was supported by the FCT project (PEst-OE/EEI/LA0009/2011).

References

Berger, J. (1985). *Statistical Decision Theory and Bayesian Analysis*. New York: Springer-Verlag.

Bertero, M. & Boccacci, P. (1998). *Introduction to Inverse Problems in Imaging*. Bristol, UK: Institute of Physics Publishing.

Besag, J. (1986). On the statistical analysis of dirty pictures. *J R Statist Soc B* **48**(3), 259–302.

Brokmann, X., Hermier, J.-P., Messin, G., Desbiolles, P., Bouchaud, J.-P. & Dahan, M. (2003). Statistical aging and nonergodicity in the fluorescence of single nanocrystals. *Phys Rev Lett* **90**(12), 120601-1.

Buades, A., Coll, B. & Morel, J.M. (2005). A review of image denoising algorithms, with a new one. *SIAM Multiscale Model Simul* **4**(2), 490–530.

Csiszáer, I. (1991). Why least squares and maximum entropy? An axiomatic approach to inference for linear inverse problems. *Ann Stat* **19**(4), 2032–2066.

Dey, N., Blanc-Féraud, L., Zimmer, C., Kam, Z., Olivo-Marin, J.-C. & Zerubia, J. (2006). Richardson-Lucy algorithm with total variation regularization for 3D confocal microscope deconvolution. *Microsc Res Tech* **69**(4), 260–266.

Didier, P., Guidoni, L. & Bardou, F. (2005). Infinite average lifetime of an unstable bright state in the green fluorescent protein. *Phys Rev Lett* **95**(9), 090602/1–4.

Dupé, F.-X., Fadili, J.M. & Starck, J.-L. (2008). Deconvolution of confocal microscopy images using proximal iteration and sparse representations. In *Proceedings of the 2008 IEEE International Symposium on Biomedical Imaging: From Nano to Macro*, Paris, France, May 14–17, 2008, pp. 736–739. Paris, France: IEEE.

Dupé, F.-X., Fadili, J.M. & Starck, J.-L. (2009). A proximal iteration for deconvolving Poisson noisy images using sparse representations. *IEEE Trans Image Process* **18**(2), 310–321.

Gavrilyuk, S., Polyutov, S., Jha, P.C., Rinkevicius, Z., Ågren, H. & Gel'mukhanov, F. (2007). Many-photon dynamics of photobleaching. *J Phys Chem* **111**(47), 11961–11975.

Geman, S. & Geman, D. (1984). Stochastic relaxation, Gibbs distributions, and the bayesian restoration of images. *IEEE Trans Pattern Anal Mach Intell* **6**, 721–741.

Jackson, D.A., Iborra, F.J., Manders, E.M. & Cook, P.R. (1998). Numbers and organization of RNA polymerases, nascent transcripts, and transcription units in hela nuclei. *Mol Biol Cell* **9**, 1523–1536.

Kempen, G.M.P., Vliet, L.J. & Verveer, P.J. (1997). Application of image restoration methods for confocal fluorescence microscopy. In *Proc SPIE, 3-D Microscopy: Image Acquisition and Processing IV*, vol. 2984, Wilson, T., Cogswell, C.J. & Conchello, J.-A. (Eds.), pp. 114–124. San Jose, CA: SPIE.

Lichtman, J.W. & Conchello, J.-A. (2005). Fluorescence microscopy. *Nat Methods* **2**, 910–919.

Molenaar, C., Abdulle, A., Gena, A., Tanke, H.J. & Dirks, R.W. (2004). Apoly(a)+ RNAs roam the cell nucleus and pass through speckle domains in transcriptionally active and inactive cells. *J Cell Biol* **165**, 191–202.

Moon, T.K. & Stirling, W.C. (2000). *Mathematical Methods and Algorithms for Signal Processing*. Englewood Cliffs, NJ: Prentice-Hall.

Rino, J., Braga, J., Henriques, R. & Carmo-Fonseca, M. (2009). Frontiers in fluorescence microscopy. *Int J Dev Biol* **53**, 1569–1579.

Rodrigues, I. & Sanches, J. (2010*a*). Photoblinking/photobleaching differential equation for intensity decay of fluorescence microscopy images, *IEEE International Symposium on Biomedical Imaging (ISBI)*, April 14–17, Rotterdam, the Netherlands.

Rodrigues, I. & Sanches, J. (2010*b*). Convex total variation denoising of Poisson fluorescence confocal images with anisotropic filtering. *IEEE Trans Image Process* **20**(1), 146–160.

Rodríguez, P. & Wohlberg, B. (2009). Efficient minimization method for a generalized total variation functional. *IEEE Trans Image Process* **18**(2), 322–332.

Sanches, J.M. & Marques, J.S. (2003). Joint image registration and volume reconstruction for 3D ultrasound. *Pattern Recogn Lett* **24**(4–5), 791–800.

Schuster, J., Brabandt, J. & Borczyskowski, C. (2007). Discrimination of photoblinking and photobleaching on the single molecule level. *J Lumin* **127**(1), 224–229.

Tomasi, C. & Manduchi, R. (1998). Bilateral filtering for gray and color images. In *ICCV '98: Proceedings of the Sixth International Conference on Computer Vision*, pp. 839–846, Washington, DC: IEEE Computer Society.

Underwood, R. (2007). *Frap and Flip, Photobleaching Technique to Reveal Cell Dynamics*. Nikon. Available at http://nikon.com/products/instruments/bioscience-applications/application-notes/pdf/nikon_note_3nn06_8_07_lr.pdf.

Vargas, D.Y., Raj, A., Marras, S.A., Kramer, F.R. & Tyagi, S. (2005). Mechanism of mRNA transport in the nucleus. *Proc Natl Acad Sci USA* **102**, 17008–17013.

Vicente, N.B., Zamboni, J.E.D., Adur, J.F., Paravani, E.V. & Casco, V.H. (2007). Photobleaching correction in fluorescence microscopy images. *J Phys Condens Matter* **90**, 1–8.

Willett, R.M. (2006). Statistical analysis of photon-limited astronomical signals and images. In *Statistical Challenges in Modern Astronomy IV* (SCMA IV), Babu, G.J. & Feigelson, E.D. (Eds.), vol. 371, pp. 247–264, Pennsylvania State University.

Willett, R.M. & Nowak, R.D. (2004*a*). Fast multiresolution photon-limited image reconstruction. In *2004 IEEE International Symposium on Biomedical Imaging: Nano to Macro*, vol. 2, pp. 1192–1195, Arlington, VA.

Willett, R.M. & Nowak, R.D. (2004*b*). Fast, near-optimal, multiresolution estimation of Poisson signals and images. In *EUSIPCO (XII European Signal Processing Conference)*, Vienna, Austria, pp. 1055–1058.

Zondervan, R., Kulzer, F., Kolchenko, M.A. & Orrit, M. (2004). Photobleaching of rhodamine 6g in poly(vinyl alcohol) at the ensemble and single-molecule levels. *J Phys Chem A* **108**(10), 1657–1665.

Appendix: Denoising Algorithm

In this appendix the PBPB model is explicitly taken into account and included in the denoising algorithm described by Rodrigues and Sanches (2010*b*).

A sequence of CLSM images of a specimen is the result of a photon detection counting process of the fluorescent molecule's emitted radiation. One of the main physical limitations of this process stems from the random nature of the photon emission and detection, especially under low illumination conditions, giving rise to a very severe nonstationary noise problem acting upon spatial and temporal varying cell features. Thus, due to the nature of the detection process, the noise corrupting these images is neither Gaussian nor additive, well described by a Poisson process. In addition, the overall image intensity decays along the experiment time due to the PBPB effects.

An image sequence, e.g., CLSM, consists of L images, $N \times M$ pixels each, acquired along the experiment time. These data can be represented as a 3D tensor, $Y = \{y_{i,j,t}\}$, where $(i, j, t) \in \Xi \times T$ are the coordinates of each point in the sequence, in pixel units, $T = \{0,1,\ldots,L-1\}, \Xi = (I \times J) \cap \Omega$, with $I = \{0,1,\ldots,N-1\}, J = \{0,1,\ldots,M-1\}$ and Ω is the region of interest in the image. Each of these image sequences can be thought of as an intensity field lying on a 3D lattice where each node is a site of the lattice. Let X be a tensor with the same dimensions of Y representing the original unknown morphology. By assuming statistical independence of the pixels, the observation model is

$$P(Y|X) = \prod_i p(y_i|x_i), \tag{A.1}$$

where $p(y_i|x_i) = (x_i^{y_i}/y_i!)e^{-x_i}$ is a Poisson distribution.

The MAP estimation of X can be formulated according the following optimization problem:

$$\hat{x} = \arg\min_X E(X,Y), \tag{A.2}$$

where the energy function, $E(X,Y) = -\log p(Y,X)$, can be written as a sum of two terms:

$$E(X,Y) = E_Y(X,Y) + E_X(X). \tag{A.3}$$

The first term, $E_Y(X,Y) = -\log p(Y|X)$, pushes the solution toward the observations and the second term, $E_X(X) = -\log p(X)$, regularizes the solution according to some previous knowledge or belief about the specimen structure, X (Moon & Stirling, 2000; Sanches & Marques, 2003).

Observation Model

Due to the quantum nature of light, the CLSM image degradation is mostly caused by the so-called shot noise, making the Poisson distribution suitable to describe the image intensity at each pixel which, according to Kempen et al. (1997), is proportional to the number of detected photons during the acquisition process. This type of multiplicative noise is referred in the literature as photon-limited (Willett, 2006) since the quality of the image is mainly determined by the number of detected photons, unless other sources of noise, such as electronic noise, are considered. Nevertheless, in modern CLSM equipment these additional sources of noise can in general be neglected when compared to the damaging effect of the Poisson noise.

Each observation, $y_{i,j,t}$, assumed corrupted with Poisson noise, exhibits a time intensity decrease due to the PBPB effects that is modeled by a weighted sum of two decaying exponentials with constant rates, λ_1 and λ_2, as derived in the Photobleaching/Photoblinking Model section and is denoted by $\eta(t,\Theta)$.

Each point of the noiseless sequence, X, in equation (A.3) can then be written as

$$x_{i,j,t} = f_{i,j,t}\,\eta(t,\Theta), \tag{A.4}$$

where $F = \{f_{i,j,t}\}$, with $(i,j,t) \in \Xi \times T$, stands for the spatiotemporal variations underlying morphology of the specimen. The parameters $\Theta = [\psi_1, \psi_2, \lambda_1, \lambda_2]$ are estimated by fitting the standardized average intensities of the images, $\overline{Y}(t)$, of the noisy data sequence, to the intensity decay model.

$$\overline{Y}(t) \approx \eta(t,\Theta) = \psi_1 e^{-\lambda_1 t} + \psi_2 e^{-\lambda_2 t}. \tag{A.5}$$

Thus, instead of estimating X from Y, as in our previous method (Rodrigues & Sanches, 2010*b*), the morphology tensor, F, is estimated by solving the following energy optimization problem:

$$\hat{F} = \arg\min_{F} E(F,Y,\Theta), \tag{A.6}$$

where $E(F,Y,\Theta) = E_Y(F,Y,\Theta) + E_F(F)$.

Therefore, the new Data Fidelity Term that takes into account explicitly the PBPB model is

$$E_Y(F,Y,\Theta) = -\log\left[\prod_{(i,j,t)\in\Xi\times T}^{N-1,M-1,L-1} p(y_{i,j,t}|f_{i,j,t},\Theta)\right], \tag{A.7}$$

where

$$p(y_{i,j,y}|f_{i,j,t},\Theta) = \frac{(f_{i,j,t}\hat{\eta}_t)^{y_{i,j,t}}}{y_{i,j,t}!}\, e^{-f_{i,j,t}\hat{\eta}_t} \tag{A.8}$$

is the Poisson distribution. $\eta(t)$, defined in equation (A.5), models the PBPB effects. Therefore,

$$E_Y(F,Y,\Theta) = \sum_{i,j,t}\left[\, f_{i,j,t}\hat{\eta}_t - y_{i,j,t}(\log f_{i,j,t} + \log\hat{\eta}_t)\right]. \tag{A.9}$$

Regularization Term

As proposed in Besag (1986), F is modeled as a Markov random field and therefore $p(F)$ is the following Gibbs distribution function (Geman & Geman, 1984):

$$p(F) = \frac{1}{Z}\, e^{-\sum_{c\in C} V_c(F)}, \tag{A.10}$$

where Z is the normalizing constant, $V_c(.)$ are clique potentials (Geman & Geman, 1984) and $E_F(F) = \sum_{c\in C} V_c(F)$ is called the Gibbs energy. The log potential functions *TV* log and L_1 log, used here in the space and temporal domains, are respectively:

$$V_{c,S}(i,j,t) = \sqrt{\log^2\left(\frac{f_{i,j,t}}{f_{i-1,j,t}}\right) + \log^2\left(\frac{f_{i,j,t}}{f_{i,j-1,t}}\right)},$$

$$V_{c,t}(i,j,t) = \left|\log\left(\frac{f_{i,j,t}}{f_{i,j,t-1}}\right)\right|. \tag{A.11}$$

Optimization

The overall energy function to be minimized is

$$\begin{aligned} E(F,Y,\Theta) = {} & \sum_{i,j,t}\left[\, f_{i,j,t}\hat{\eta}_t - y_{i,j,t}(\log(f_{i,j,t}) + \log\hat{\eta}_t)\right] \\ & + \alpha\sum_{i,j,t}\sqrt{\log^2\left(\frac{f_{i,j,t}}{f_{i-1,j,t}}\right) + \log^2\left(\frac{f_{i,j,t}}{f_{i,j-1,t}}\right)} \\ & + \beta\sum_{i,j,t}\left|\log\left(\frac{f_{i,j,t}}{f_{i,j,t-1}}\right)\right|, \end{aligned} \tag{A.12}$$

where α and β are strictly positive image dependent or constant tuning parameters to reduce or increase the strength of the regularization in the spatial and temporal dimensions, respectively.

The nonconvex energy function equation (A.12) can become convex if the following change variable is used:

$$Z = \log(F), \tag{A.13}$$

which leads to the following energy function:

$$E(F,Y,\Theta) = \sum_{i,j,t} [e^{z_{i,j,t}}\hat{\eta}_t - y_{i,j,t}(z_{i,j,t} + \log \hat{\eta}_t)] + \alpha \sum_{i,j,t} \sqrt{(z_{i,j,t} - z_{i-1,j,t})^2 + (z_{i,j,t} - z_{i,j-1,t})^2} + \beta \sum_{i,j,t} |z_{i,j,t} - z_{i,j,t-1}|. \quad (A.14)$$

The morphology estimation, $\hat{F}$, is the minimizer of equation (A.14), $\hat{Z}$, by reverting equation (A.13):

$$\hat{F} = e^{\hat{Z}}. \quad (A.15)$$

The minimization of equation (A.14), accomplished by finding its stationary point with respect to each $z_{i,j,t}$, is performed by using the Newton's algorithm and an IRWLS-based procedure (Rodríguez & Wohlberg, 2009) to circumvent nonlinearity and to promote convergence, which gives

$$\hat{Z}^{(k)} = \hat{Z}^{(k-1)} - (e^{\hat{Z}^{(k-1)}}\hat{\eta} - Y + H^{(k-1)}/D^{(k-1)}), \quad (A.16)$$

where (k) is the iteration number and $(/)$ denotes the component-wise division. The elements of $D^{(k)} = \{d^{(k)}_{i,j,t}\}$ are

$$d^{(k)}_{i,j,t} = e^{z^{(k)}_{i,j,t}}\hat{\eta}_t + \phi^{(k)}_{i,j,t}, \quad (A.17)$$

and the elements of $H^{(k)} = \{h^{(k)}_{i,j,t}\}$ are

$$h^{k}_{i,j,t} = (\Phi * \hat{Z}^{(k)})_{i,j,t}. \quad (A.18)$$

The 3D mask $\Phi_{i,j,t}$ is

$$\Phi_{i,j,t} = 2\begin{pmatrix} 0 & 0 & 0 \\ 0 & -\beta v_{i,j,t} & 0 \\ 0 & 0 & 0 \\ 0 & -\alpha\omega_{i,j,t} & 0 \\ -\alpha\omega_{i,j,t} & \phi_{i,j,t} & -\alpha\omega_{i,j+1,t} \\ 0 & -\alpha\omega_{i+1,j,t} & 0 \\ 0 & 0 & 0 \\ 0 & -\beta v_{i,j,t+1} & 0 \\ 0 & 0 & 0 \end{pmatrix}, \quad (A.19)$$

where

$$\phi_{i,j,t} = \alpha[2w_{i,j,t} + w_{i+1,j,t} + w_{i,j+1,t}] + \beta[v_{i,j,t} + v_{i,j,t+1}],$$

$$w(z^*_{i,j,t}) = \frac{1}{\sqrt{(z^*_{i,j,t} - z^*_{i-1,j,t})^2 + (z^*_{i,j,t} - z^*_{i,j-1,t})^2} + \varepsilon},$$

$$v(z^*_{i,j,t}) = \frac{1}{|z^*_{i,j,t} - z^*_{i,j,t}| + \varepsilon}. \quad (A.20)$$

$\varepsilon = 10^{-6}$ is a small number to avoid division by zero. Since the true solution to this problem, Z^*, is not known in each iteration (k), the values for $Z^{(k-1)}$ are used instead (see Rodrigues & Sanches, 2010*b* for more details).